NUMERICAL SIMULATION OF THE UNSTEADY SLIPSTREAM OF LIFT AUGMENTING DISTRIBUTED PROPELLERS

Mário Firnhaber Beckers*, Michael Schollenberger*, Thorsten Lutz*

* University of Stuttgart, Institute of Aerodynamics and Gas Dynamics,
Pfaffenwaldring 21, 70569 Stuttgart, Germany

Abstract

Unsteady propeller-wing interaction effects of a distributed propulsion system in a high-lift case (lift coefficient of about 10) were investigated via unsteady Reynolds-averaged Navier–Stokes simulations. In a first stage, the turbulence model and time step were examined. The Spalart–Allmaras turbulence model was found to be the least dissipative model. The unsteady interaction effects were identified by isolating them from the steady-state effects. They are dominated by the behaviour and influence of the blade tip vortices, which was analysed in detail. However, the influence of the unsteady effects on the integral performance of the propeller-wing system was found to be negligible compared to the steady-state effects. The initial slipstream development process was simulated, revealing a duration of about 85 to 90 propeller revolutions until a periodic state is reached in this high-lift scenario. Different methods of representing the unsteady propeller motion were investigated and compared: fully resolved blades and the Actuator Line model. The latter proved to be significantly less computationally expensive, especially when the initial slipstream development process is skipped via an initial Actuator Disk simulation, with only about 12.5% of the computation cost of the fully resolved simulation.

Keywords

Distributed Electric Propulsion; High-Lift; Computational Fluid Dynamics

NOMENCLATURE

Symbols

α	wing angle of attack	deg
U_∞	farfield flow velocity	m/s
C_D	wing drag coefficient	-
$C_{F,ex}$	excess thrust coefficient	-
$C_{F,inf}$	thrust coefficient in inflow direction	-
C_L	wing lift coefficient	-
$C_{L,eff}$	effective lift coefficient	-
C_P	propeller power coefficient	-
c_p	pressure coefficient	-
C_T, C_F	propeller thrust coefficients	-
D	propeller diameter	m
J	propeller advance ratio	-
R	propeller radius	m
c	wing chord length (clean config.)	m
Ω	propeller rotational speed	rpm
S	wing segment reference area	m^2
N	time	rev

Abbreviations

ACD	actuator disk
ACL	actuator line
CFD	computational fluid dynamics
DEP	distributed electric propulsion
URANS	unsteady Reynolds-averaged Navier–Stokes

1. INTRODUCTION

The aerodynamic interaction between propellers and a wing is a highly complex phenomenon of various aerodynamic effects that depends on many geometrical and operational parameters [1–5]. Understanding these effects is important to assess the potential of aircraft technologies featuring strong aero-propulsive coupling, such as distributed electric propulsion (DEP). In addition to the already complex propeller-wing interactions, a DEP system also features the interaction between adjacent propellers (propeller-propeller interactions). DEP is considered a promising technology for the future (partial) electrification of air mobility [6], due to a possible reduction of total energy consumption of a flight mission. The relevant aerodynamic interactions are therefore currently being investigated in multiple research projects across several facilities.

Comprehensive research on propeller-wing interactions is being carried out at Delft University of Technology (TU Delft). Foundational work on propeller-wing interactions was performed by Veldhuis [1] and more recently by Sinnige [2] and Stokkermans [3]. Currently, the aerodynamic perspective of propeller-wing interactions in high-lift cases is being investigated experimentally by Duivenvoorden [7] and numerically by Ribeiro [8]. The application of propellers for both propulsive and recuperation purposes is being investigated by Nederlof [9] from an aerodynamic perspective and by Goyal [10] with an aeroacoustic focus. However, these detailed analyses focus on the propeller-wing interactions with a single propeller, e.g. a wingtip-mounted propeller, or even isolated propellers. The propeller-propeller interactions are therefore not captured and require expanding research in order to understand the full aerodynamics of DEP systems. Research on the aerodynamics of DEP systems (including propeller-propeller interactions) was conducted at NASA and Georgia Institute of Technology as part of the X-57 Maxwell project (previously LEAPTech), e.g. by Deere [11] and Patterson [12], developing a new type of propeller blade design for lift augmentation purposes and analysing the resulting performance of the DEP technology in a high-lift case. In the Clean Sky 2 project CICLOP, DEP systems are investigated via CFD simulations [13] and wind tunnel experiments of a three-propeller setup [14]. Findings include the sensitivity of the lift augmentation on the propeller position [14] and the thrust setting [13]. It was also found that dynamic load fluctuations are mostly concentrated on the area near the leading edge (suction peak and stagnation point) [14].

The Clean Sky 2 project DISPROP focuses on the high-lift aspect of DEP systems. Similarly to the CICLOP project, both numerical investigations and wind tunnel experiments are performed and combined. In the early stages of DISPROP, the sensitivity of the interaction effects to the propeller position was investigated numerically [4] in order to identify suitable positions for the wind tunnel experiments. The results of the wind tunnel experiments [15] can then be called upon for the validation of the numerical methods [16]. Another numerical parametric study has demonstrated the influence of the flight case and propeller operation settings, e.g. the propeller thrust, on the resulting lift augmentation [5]. The unsteady interaction effects are also investigated as part of DISPROP: Wickersheim [17] carried out a comparison of the two unsteady methods of representing propellers (Actuator Line and fully resolved propeller blades) with regard to the similarity of aeroacoustic predictions. A similar comparison of methods, however focusing on the aerodynamic aspects in cruise conditions, was previously done by Schollenberger [18] as part of the ELFLEAN research project.

The goal of the present study is to investigate the unsteady interaction effects (propeller-wing and propeller-propeller) of a complex high-lift case in detail, from an aerodynamic (i.e. not acoustic) perspective. An additional goal is to verify the accuracy and the benefits of the Actuator Line model implemented into TAU by Schollenberger [19] when applied in such a complex case.

2. METHODOLOGY

The present investigation is carried out in order to determine best practices regarding the unsteady CFD simulation of distributed propulsion systems in high lift conditions. A particularly complex case was selected for this: large propeller thrust resulting in strong interaction effects, such as especially large lift augmentation. It is assumed that good results for this case indicate that the setup is also applicable to less complex cases (e.g. lower thrust).

The numerical simulations were performed using the flow solver TAU [20], developed by the German Aerospace Center (DLR). Unsteady Reynolds–Averaged-Navier–Stokes equations (URANS) are solved in a Roe 2nd order Upwind Finite Volume scheme. The increased numerical dissipation of Upwind schemes at low Mach numbers is mitigated using a correction by Thornber [21]. The flow is assumed to be fully turbulent. The selection of a suitable turbulence model is part of the present investigation. An implicit time stepping scheme is employed, where the inner iteration loop of a time step is considered converged via a Cauchy criterion (relative C_L and C_D fluctuations across 50 iterations under 0.0001% and 0.001%, respectively) and is otherwise limited to 1000 iterations.

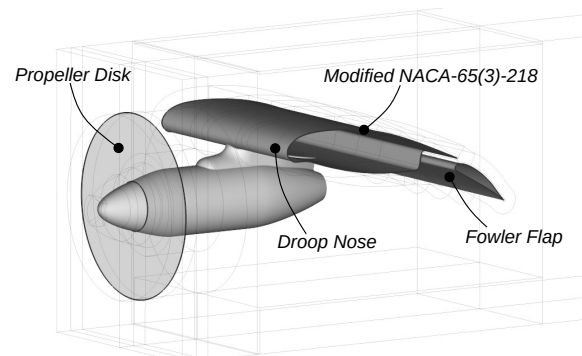### 2.1. Geometry & Operation settings

FIG 1. Propeller-wing system geometry

The considered geometry is visualized in Figure 1. It is an idealised 2.5D distributed propulsion system, composed of a wing segment coupled with a single tractor propeller. Unlike in previous 2.5D DISPROP investigations [4, 5], a propeller nacelle and a pylon, designed at TU Braunschweig, are implemented and connect the propeller to the wing segment. Periodic boundary conditions are applied at the side boundaries of the computational domain. Thus, an infinitely extruded wing with an infinite number of co-rotating distributed propellers is effectively considered.

The wing segment is rectangular, with a constant airfoil geometry. This airfoil is derived from the NACA-65(3)-218 airfoil, which was modified to include a Fowler Flap and a Droop Nose. The Fowler Flap geometry was provided to the DISPROP project by Airbus Defence and Space, whereas the Droop Nose geometry was designed at TU Braunschweig at the beginning of the project [16, 22]. The propeller geometry is based on the six-bladed TUD-XPROP propeller [3], which was provided to the DISPROP project by TU Delft. The propeller was scaled to $D=550mm$ and additionally modified to feature a larger spinner radius (inner disk radius $r_i=26.66\%R$), which was necessary due to mechanical constraints.

Parameter	Value
Clean chord length c	688 mm
Propeller Diameter D	550 mm
Streamwise Position X_p	-40 %c
Vertical Position Z_p	-90 %R
Propeller Inclination θ	10 deg
Spanwise propeller spacing ΔY_{tip}	20 %D

TAB 1. Geometry parameters

Information on the specific propeller position is listed in Table 1. This propeller position was selected as one of three positions to be considered in the DISPROP project as part of an earlier parametric investigation [4], where it yielded the most promising results regarding lift augmentation. However, the position was determined for a different operation setting (J=0.791). Another previous parametric study in DISPROP [5] has shown a significant impact of the operation setting (e.g. thrust) on the optimal propeller position. The propeller is thus not located in its optimal position for this specific operation case, and a higher propeller position would likely lead to more beneficial results. Nonetheless, this propeller position (Pos 3, see [4]) was selected for the present study for a better comparison to wind tunnel data and to avoid a specific nacelle and pylon redesign.

Parameter	Value
Inflow Velocity U_∞	20 m/s
Rotational Speed Ω	6896 rpm
Advance Ratio J	0.316
Thrust coefficient C_T	0.32
Angle of Attack α	14 deg

TAB 2. Operation parameters

As mentioned above, the propeller is operated in an off-design case, which is aimed to represent a Short Take-off and Landing (STOL) case. The advance ratio is greatly decreased compared to the design case ($J=0.316$ vs $J=0.791$) via reduction of the inflow velocity U_∞, while the thrust coefficient is increased ($C_T=0.32$ vs $C_T=0.3$). This leads to an operation scenario with a very large disk loading resulting in strong interaction effects, e.g. large lift augmentation. The full information of the operation settings is listed in Table 2.

2.2. Propeller implementation

Several options are available in TAU to represent a propeller. Besides the direct representation of the propeller blades, incl. resolving the boundary layer and thus the viscous effects, there are two boundary condition based approaches via introduction of a force distribution: the steady-state Actuator Disk (ACD) method, implemented into TAU by Raichle et al [23], and the unsteady Actuator Line (ACL) method, implemented into TAU by Schollenberger et al [19]. With the ACL the individual propeller blades are approximated by line loads rotating in time. In the present study, the two unsteady propeller methods are primarily employed: the direct representation of propeller blades (henceforth referred to as "fully resolved blades") and the Actuator Line (ACL) method. In a single simulation, the Actuator Disk (ACD) method is also employed. The motion of the fully resolved blades is accomplished via the CHIMERA method [24]. Employing a boundary condition based approach (ACD or ACL), where a single two-dimensional disk represents the entire propeller, requires input data regarding the appropriate reaction of the modelled propeller to the local flow conditions. In the case of this study, a Blade Element theory based approach is employed, which is already implemented in TAU [23]. This approach determines the local flow angle and calculates the blade reaction force based on (position-dependent) polar data, which is provided by the user as input. Naturally, this modelling approach will lead to some loss in accuracy. However, not resolving the boundary layer of each blade leads to a significant decrease in the number of cells for the CFD mesh [18], which will be discussed in the following chapter.

2.3. CFD mesh

The CFD meshes utilized in the present study were created with the program Pointwise [25]. The "main mesh" (used in the Actuator Line approach) is visualized in Figure 2 in two cuts: $Y=0$, to visualize the streamwise cell distribution, and $X=10\%c$, to visualize the radial cell distribution. The main mesh topology was taken from previous 2.5D investigations [4]. It includes a streamwise-extruded propeller block, two spanwise-extruded blocks for the wake and main part of the wing boundary layer and an unstructured block connecting the three extruded blocks. This topology was modified to include the nacelle and pylon geometry, which are now embedded into the unstructured connection block. The boundary layer of the nacelle and pylon geometry is extruded using the T-Rex method in Pointwise. In order to reduce numerical dissipation inside the unstructured block, the remaining volume is filled with hexahedral cells via
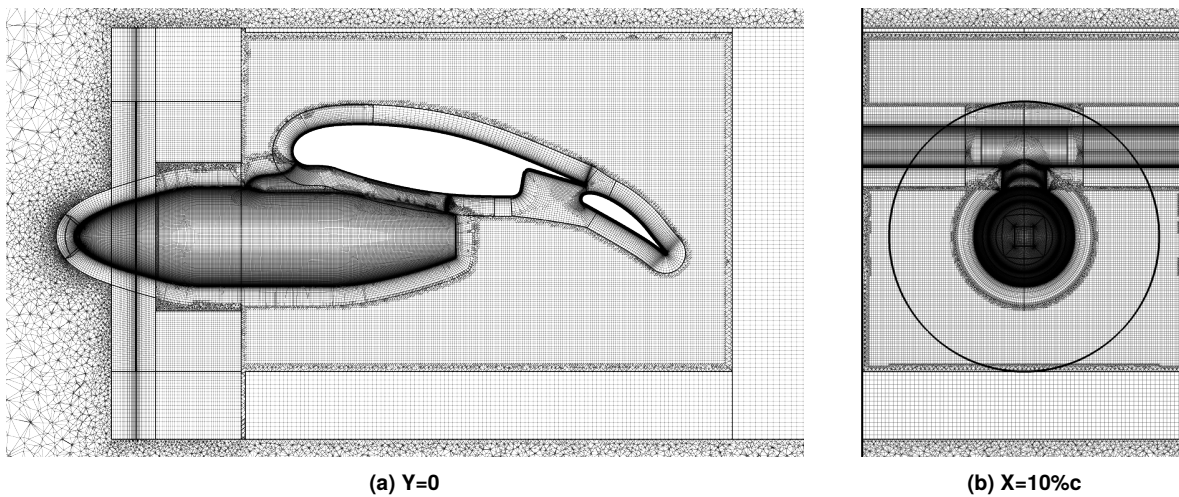
(a) Y=0

(b) X=10%c

FIG 2. CFD mesh visualization

the Voxel method in Pointwise. The Voxel algorithm is limited to a single cell size in order to avoid transition layers, which also introduce significant numerical dissipation. This single Voxel cell size was determined in a preliminary study, with respect to the ability to capture the blade tip vortices. The boundaries of the unstructured Voxel block were moved compared to the original mesh topology from previous investigations, in order to also prevent the blade tip vortices from passing the transition layer between blocks. A global mesh refinement study was not performed. Cell sizes were selected based on previous investigations and several individual preliminary studies, e.g. one regarding the Voxel cell size. The cost and effort of a global mesh refinement study for such a complex case was considered disproportionate compared to the insight it would provide. A selection of parameters from the main (ACL) mesh is listed in Table 3.

Number of cells	23,869,059
Points on airfoil (main / Fowler)	322 / 197
Points on propeller disk	
in radial direction	93
in circumferential direction	198
Voxel cell size = spanwise spacing	$4.32mm$

TAB 3. Selection of main (ACL) mesh parameters

The mesh of the fully resolved blade simulations is divided into two parts: 1) the background mesh based on the main ACL mesh and 2) a rotating propeller mesh. For the background mesh, the main mesh is modified in the area surrounding the propeller via local refinements, introducing the CHIMERA overlap and cutting the required hole. The rotating propeller mesh encompasses a cylinder with the six propeller blades and their boundary layers as well as the spinner boundary layer. In total, the full mesh has a size of 33,396,648 cells (background: 26,691,275; propeller: 6,705,373), which represents an increase by ~40% compared to the ACL counterpart.

3. STUDIES & RESULTS

The goals of the present investigation are to provide best practices for the unsteady simulation of propeller-wing interactions in a high-lift case and to analyse the resulting interaction effects themselves, including the start-up process of the propeller slipstream. In addition, three different methods of representing the unsteady propeller slipstream are investigated:

1) Fully-resolved blades, restarted from a steady-state zero-thrust solution: the slipstream develops with time after the simulation is initialized with a zero-thrust solution.
2) Actuator Line, restarted from a steady-state zero-thrust solution ("ACL-startup"): the slipstream develops with time after the simulation is initialized with a zero-thrust solution.
3) Actuator Line, restarted from a steady-state Actuator Disk solution ("ACL-boosted"): the steady-state slipstream is already developed from the Actuator Disk simulation.

The initial part of the investigation explores different parameters of the numerical URANS simulation. This analysis is done for the least resource ACL-boosted intensive case. The second part of the investigation examines the unsteady interaction effects occurring in the ACL-boosted case. The third part consists of a detailed comparison of the three unsteady propeller representation methods, considering multiple aspects: integral values, flow physics and required computational resources. To expand the analysis of the integral performance, an additional simulation with the ACD model with the same simulation setup of the ACL-boosted case was performed.

3.1. Numerical setup variation

Two aspects of the numerical setup are varied in this investigation: the turbulence model and the time step. The results of the variations and the impacts of these two aspects on the unsteady simulation of high-lift propeller-wing interaction effects are detailed in the following section. Best practices are then derived.

3.1.1. Turbulence Model

The following turbulence models were selected for the present study:

1) Spalart–Allmaras model in negative formulation [26] (SA-neg): this is the default turbulence model in TAU.
2) Spalart–Allmaras model with rotation/curvature correction by Shur [27] (SA-RC): the SA-neg formulation was selected as the baseline and the rotation/curvature correction was activated.
3) Menter-SST model in original formulation [28].
4) Wilcox k-ω model in original formulation [29].

With each of these turbulence models a run of 12 propeller revolutions was simulated. The simulations were initialized with the results of an Actuator Disk simulation (ACL-boosted). The initialization simulation was run with a first-order Roe Upwind scheme (with Thornber correction [21]) over 20000 iterations. Only one initialization simulation was performed, using the SA-neg turbulence model. The resulting flow field was utilized as a starting point for all the unsteady ACL runs with the different turbulence models.

(a) Lift coefficient (surface integral only)

(b) Drag coefficient (surface integral only)
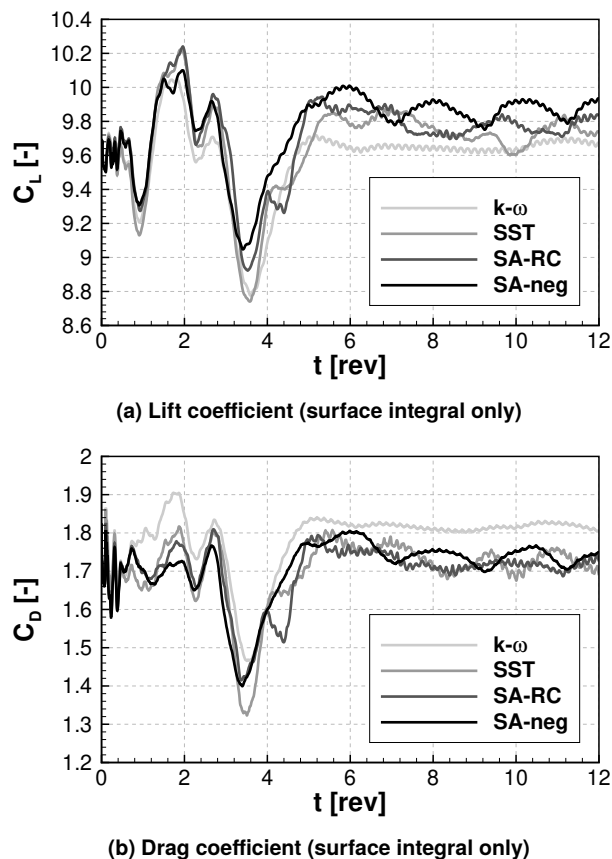
FIG 3. Turbulence Model comparison: Development of lift and drag coefficients over time

The development of the lift and drag coefficients over the simulated physical time is plotted in Figure 3. These plots show that about 5 revolutions are required as an initialization of the unsteady effects. After about 8 revolutions the slipstream appears to be developed. The SA-neg turbulence model simulation enters a clear periodic state, with two dominant periodic components: a ~0.5P oscillation (i.e. with a period of about 2 revolutions) superimposed with a 6P oscillation (i.e. with a period of 1/6th rotation, the blade-passing frequency). The 6P oscillation is present across all turbulence models. The lower frequency fluctuations are more complex with the other turbulence models, possibly indicating that the simulations have not yet reached their periodic state, unlike the SA-neg simulation.
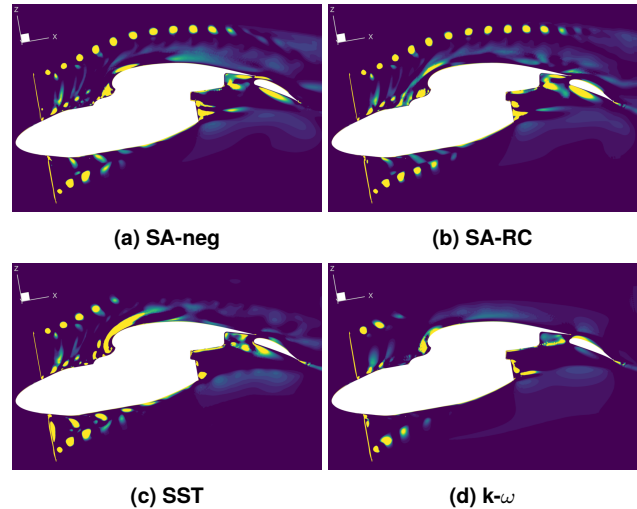

(a) SA-neg   **(b) SA-RC**

(c) SST   **(d) k-ω**

FIG 4. Turbulence Model comparison: Q criterion distribution in Y=0 cut (yellow: Q=200000)

An important effect to be captured by unsteady propeller simulations is the blade tip vortex. The ability of a simulation to preserve and capture the movement of the blade tip vortices is a sign of low numerical dissipation and thus an indicator of the quality of the simulation. The different turbulence models are therefore also evaluated with respect to their ability in capturing and tracking the blade tip vortices. The distributions of the Q criterion in the Y=0 cut for the different turbulence models are shown in Figure 4. The results show that for the k-ω turbulence model, the blade tip vortices are only preserved for about one half revolution downstream of the propeller. With the Menter-SST model, the vortices are preserved for about one full revolution. It can be seen that the blade tip vortices on the suction side are preserved slightly longer than on the pressure side. With both Spalart–Allmaras (SA) turbulence models, the blade tip vortices on the suction side reach the trailing edge of the main element until they dissipate. However, the discrepancy between suction side and pressure side is much more pronounced here. Compared to the Menter-SST model, the vortices on the pressure side are preserved for a similar length. The significant difference is only found on the suction side. When comparing the two SA models, the SA-RC model has a minor advantage in terms of vortex preservation. On both the pressure and the suction sides, the vortices are preserved slightly longer (about one "lattice" on each side). However, this difference is relatively small when comparing to the other two models.

Lastly, the four turbulence models are compared with respect to the required computational resources. The number of calculated iterations and the required computational resources (specified in core-hours) are listed in Table 4. The two-equation models require more resources than the one-equation models, which was expected due to the inclusion of an additional transport equation. However, the increase in computation cost is not only due to the additional transport equation but also due to a larger number of calculated iterations, by about 15-25%. It appears that more iterations need to be calculated to reach convergence of the inner loops (per time step) with the two-equation models. In contrast, the rotation correction does not appear to significantly influence the number of calculated iterations. However, the required computational resources are about 13% larger for the SA-RC model than for the SA-neg model. These results are in accordance with the original publication by Shur [27], where an increase in computation cost by about 20%, but no effect on convergence, is stated.

Turbulence Model	Iterations	Core-hours
SA-neg	**91,483**	**4,165 (-)**
SA-RC	92,711	4,711 (+13%)
SST	115,022	5,675 (+36%)
k-ω	104,925	4,948 (+19%)

TAB 4. Required computational resources by different turbulence models for last / 12th revolution

Based on all these findings, the Spalart–Allmaras turbulence model without rotation correction (SA-neg) was selected for the remaining studies of the present investigation. It presents a clear periodic behaviour after 8 propeller revolutions, offers comparably good preservation of the blade tip vortices and has the lowest computation cost.
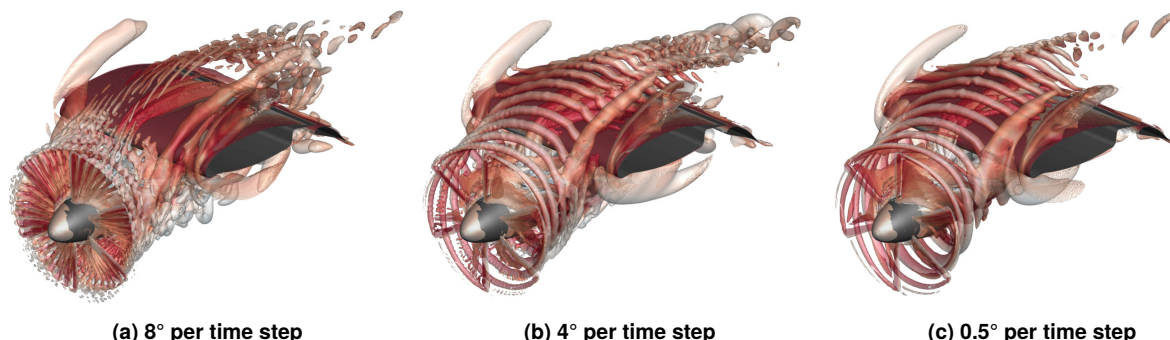
3.1.2. Time step

In the present study, the following time steps were considered: $8°$, $4°$, $2°$, $1°$, $0.5°$. The time steps are specified by the angular movement of the propeller blade in each time step, as is commonly done for propeller applications. Thus, for a time step of $1°$ the propeller blade moves by $1°$ in each time step.

Visualizations of the flow fields that develop with different time steps are presented in Figure 5. Iso-surfaces of the Q criterion are shown to highlight the different vortex patterns that develop. With a time step of $8°$, no clear blade tip vortices can be seen. In addition, the vorticity introduced by the blade, thus representing the blade wake, does not merge to a continuous sheet. The large time step prevents the formation of such continuous vorticity shapes and each introduction of vorticity flows downstream individually (henceforth referred to as "artifacts of vorticity"). With a time step of $4°$, continuous blade tip vortices and wake sheets are formed. However, some artifacts of vorticity are still present near the blades and the distribution of the blade tip vortices is not quite in agreement with the finer time steps (from $2°$ downward, only $0.5°$ shown). With the finest time step of $0.5°$, no artifacts of vorticity are found, presenting clear blade tip vortices and blade wake sheets.
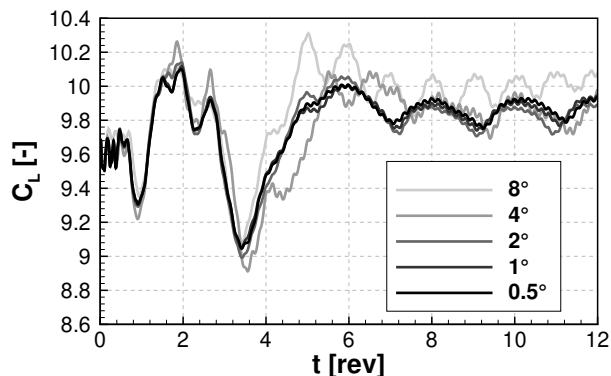
FIG 6. Time step comparison: Development of lift coefficient over time

The development of the wing lift coefficient with the different time steps is plotted in Figure 6. The curves appear to converge with decreasing time step: the curve with a time step of $2°$ already presents a very similar progression as that with a time step of $0.5°$. A clear outlier is the curve with a time step of $8°$, likely due to the inability to form continuous blade tip vortices and thus the exact unsteady flow field. With a time step of $4°$, where continuous blade tip vortices are formed, the progression of the lift coefficient is close to that of the finer time steps, but with a larger deviation than

(a) 8° per time step	(b) 4° per time step	(c) 0.5° per time step

FIG 5. Vortex visualization for different time steps: Q criterion (Q=50000), coloured by local velocity magnitude.

6

the finer time steps of $2°$ downward. This is also in accordance to the vortex pattern deviations described above. It should be said that even with the largest time step of $8°$ the magnitude of the lift coefficient is still close to that of the finer time steps. The lift coefficient thus seems to be mostly dependent on the steady-state flow field and not the unsteady flow field.
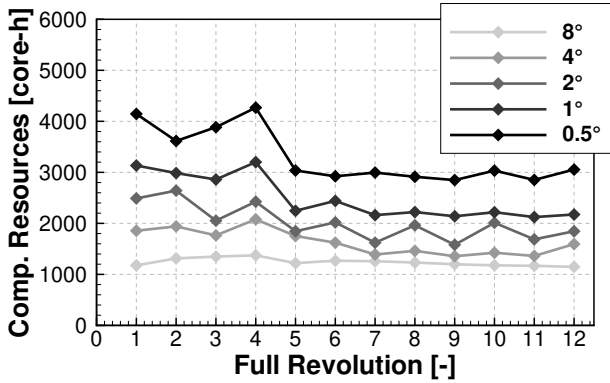

FIG 7. Time step comparison: Development of required computational resources (core-h) over number of revolution

Increasing the time step innately reduces the number of required time steps for the same total time. Therefore it is regarded as an option to reduce the computation cost of an unsteady simulation. The amount of computational resources required for each full revolution is plotted in Figure 7 for the different time steps. It can be seen that a decrease in time step from $4°$ to $0.5°$ (a reduction by factor 8) effectively doubles the computation cost of a simulation (+102%). The temporal resolution is therefore increased by a larger factor than the computation cost. However, since a time step of $2°$ achieves similar results to $0.5°$ at only about 61% of the cost, it is a valid choice to save the computational resources here due to diminishing returns. Interestingly, after 4 revolutions the computational requirements drop significantly. This effect gets stronger with decreasing time step: for a time step of $0.5°$, a drop by about 25-30% is observed. As mentioned previously, the initial development of the unsteady effects in this case takes about 4-5 revolutions. This leads to the assumption of a correlation between the phase of the initial development of the ACL-induced unsteady effects and the computation cost.

Based on all the discussed results, a time step of $2°$ or lower is recommended for the exact simulation of the unsteady effects of high-lift propeller-wing interactions, while a time step of $4°$ or lower is required to capture blade tip vortices. For the remaining studies of the present investigation, the following time steps were selected:

- $4°$ during the initialization of the flow field incl. unsteady effects (continuous blade tip vortices).
- $0.5°$ during the consequent more precise calculation of the flow field (for the highest accuracy, despite the increased computation cost).

3.2. Unsteady Interaction Effects

In the following section the unsteady interaction effects found in the ACL-boosted case (SA-neg turbulence model, $0.5°$ time step) will be discussed. A snapshot of the flow field with a visualization of the vortices is presented in Figure 8b. Two additional propellers were included in post-processing (by copying and translating the data) in order to better visualize the effects in the area between propellers.

In order to identify the unsteady effects, first the steady-state effects need to be extracted. For this, the flow field was averaged over the last 4 propeller revolutions. The equivalent visualization of the steady-state flow field is presented in Figure 8a. The following steady-state effects can be observed:

- A vorticity sheet surrounding the propeller slipstream (upstream of the wing). This vorticity sheet is deformed by the wing, moving "outwards" (towards the other propellers) and rolls up into two large vortices (one on each side) when passing over/under the wing.
- Two nacelle vortices in the center of the propeller slipstream, close to the wing surface. Other nacelle vortices also move under the wing.
- An additional vortex between the propellers, close to the wing surface, moving "inward". This vortex is created from the pressure gradients on the wing surface and effectively splits the near-wing flow into propeller-specific sections, as discussed in [4].
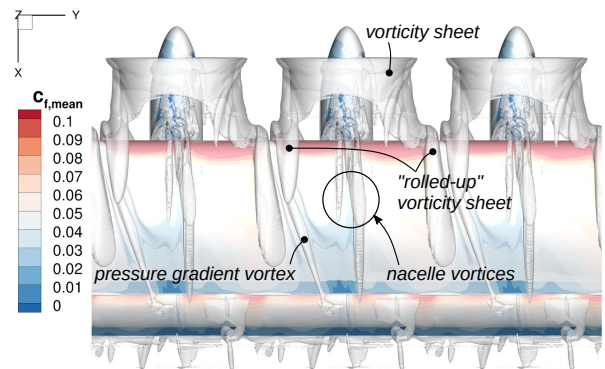
(a) Steady-state (4-rev mean), color: mean surface friction
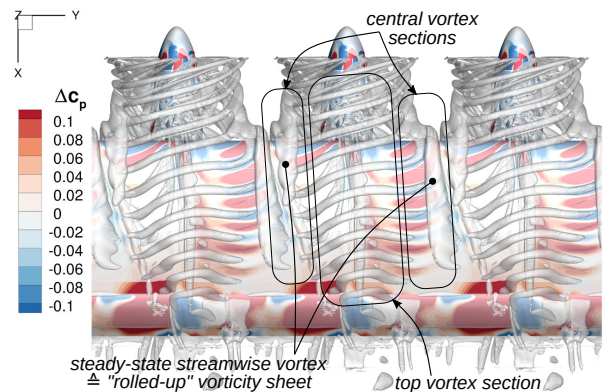
(b) Unsteady (snapshot), color: c_p deviation from mean

FIG 8. Comparison of the unsteady and mean flow: Top-down view, vortices visualized via Q criterion (Q=50000)

In the unsteady snapshot the vorticity sheet at the slip-stream edge is replaced by the discrete blade tip vortices. Depending on the section of the blade tip vortex, different behaviour is observed:

- The top section of the vortex, moving into the suction side, see Figure 4, continues to propagate downstream. When moving downstream the radius of the vortex arc appears to get smaller. Similar behaviour was observed by Ribeiro et al [8], where an "inverted-T shape" was observed in the wake of the propeller-wing system. The slipstream with reducing radius forms the upper part of the "inverted-T".

- The bottom section of the vortex, moving into the pressure side, dissipates relatively quickly, as was previously seen in Figure 4. Ribeiro et al [8] observed increased vortex mixing on the wing's pressure side with increasing lift coefficient and explained this as follows: the reduced velocity on the pressure side decreases the distance between vortices, causing them to mix and thus the decay of the discrete blade tip vortices. Due to the increased numerical dissipation of the URANS simulations in the present investigation, the small-scale vortex mixing is not visible. However, the decay of the blade tip vortices is still captured.

- The two central sections of the vortex, on the ascending and descending blade sides, are influenced greatly by the wing. The wing surface causes a stagnation of the flow, which in turn causes the slipstream and thus also the vortices on its edge to move "outwards" in spanwise direction. However, the primary direction of flow is still dominant and thus the blade tip vortices "wrap around" the wing and are stretched with increasing propagation/time. The blade tip vortices in this section therefore are dominated by a streamwise orientation as opposed to the usual circumferential orientation. Ribeiro et al [8] also observed this behaviour of the blade tip vortices moving outwards and wrapping around the wing. The stagnation effect and thus the momentum of the spanwise movement of the blade tip vortices is limited, in part due to the adjacent propellers. Therefore the blade tip vortices wrapped around the wing merge into the large steady-state streamwise vortex discussed previously, which the top section of the blade tip vortex then connects to.

In addition to the blade tip vortices, the sheets of vorticity representing the blade wake can also be observed in Figure 8b as they propagate over the wing. However, the influence seems to be relatively small compared to that of the discrete vortices.

Figure 8b also showcases the pressure fluctuations on the wing surface via the color scheme: blue coloring thereby represents a momentary pressure reduction and red coloring a momentary pressure increase compared to the mean value. It is clearly visible that as a blade tip vortex moves over the wing surface, a pressure decrease is induced on the surface. This is expected due to the orientation of the vortex that induces a velocity increase on the surface, which is generally associated with a pressure decrease.
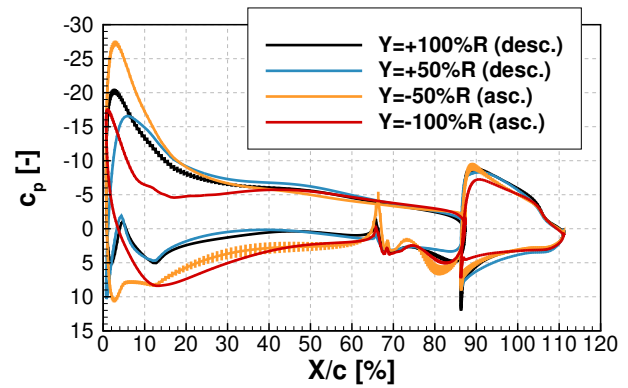

FIG 9. Pressure coefficient c_p distribution at four spanwise locations, incl. fluctuation intensity (root mean square): -100%R, -50%R, +50%R, +100%R.

Figure 10 shows the streamwise distribution of the pressure coefficient for four different spanwise locations: Y=-100%R, -50%R, +50%R, +100%R. Positive values of Y represent the descending blade side and negative values of Y the ascending blade side. The mean value is plotted and error bars are included which represent the root mean square of the pressure fluctuation. The strongest suction peak is observed at the location Y=+50%R. Of the four observed locations, this is also where the largest lift is generated. This is expected since the influence of the ascending propeller will be strongest here, causing the largest increase in dynamic pressure and also in effective angle of attack. Observing the pressure fluctuations, by far the strongest fluctuation is found on the pressure side of the Y=+50%R location. This can be explained by a strong nacelle vortex that moves under the wing at Y≈+50%R. Fluctuations in the exact position of this vortex will lead to strong pressure fluctuations at Y=+50%R. Otherwise, pressure fluctuations appear to be most prominent on the descending blade side at Y=+100%R, which is also in accordance with the snapshot displayed in Figure 8b.

3.3. Comparison of Methods

In this section, the three methods for unsteady propeller simulation are compared with regard to the ability of capturing the unsteady effects, the development of the integral performance parameters and the computation cost.

The flow fields of the respective final time step snapshots are shown in Figure 10. Vortices are displayed via the Q criterion. Blue colouring represents a steady-state vortex and red colouring a time-dependent vortex. The difference between the two ACL simulations is relatively small. Most noticeably the nacelle vortex in the center of each slipstream is positioned differently: in the ACL-boosted case the vortex is located further up (or to the right, when looking in flight direction), indicating a larger section of the wing being influenced by the ascending blade. In the fully resolved case an additional unsteady effect can be observed, leading to a significantly different vortex structure than

8

(a) Fully resolved blades   (b) Actuator Line (startup)   (c) Actuator Line (boosted)
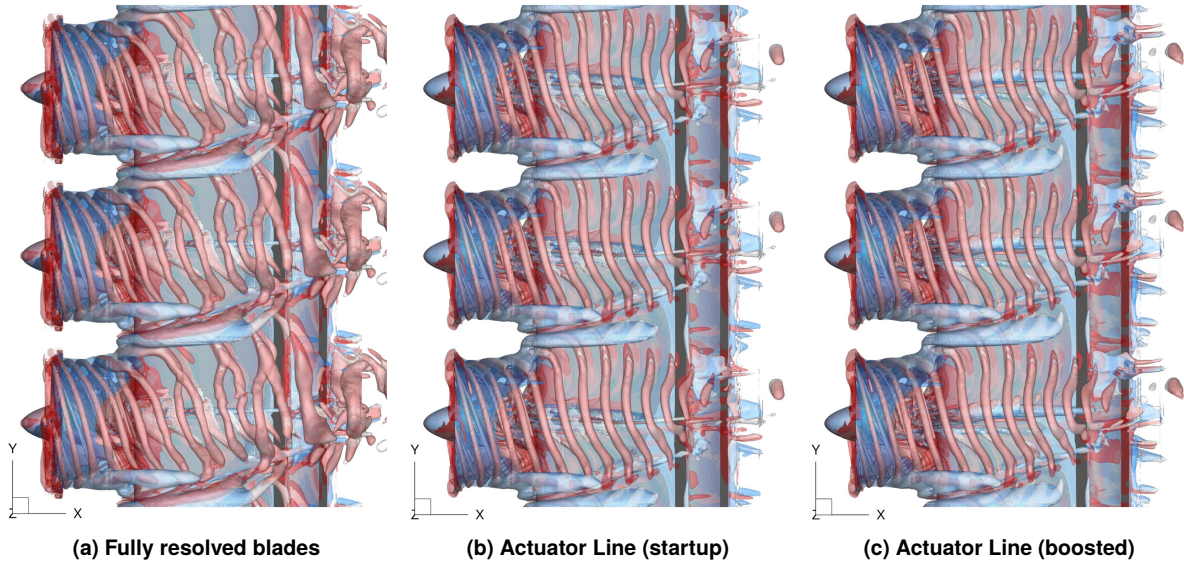
FIG 10. Flow comparison of unsteady propeller methods: Top-down view, vortices visualized via Q criterion (Q=50000, blue shading = steady-state vortices, red shading = unsteady vortices)

that seen in the two ACL simulations. This additional effect will be discussed in more detail in section 3.3.1. The integral performance of the propeller-wing configuration is described via a set of three parameters: the propeller power coefficient C_P, the effective lift $C_{L,eff}$ and the excess thrust $C_{F,ex}$. Since the thrust coefficient C_F is normalized with the same information as the lift and drag coefficients, the respective values of the same direction can be simply added. The effective lift $C_{L,eff}$ and the excess thrust $C_{F,ex}$ are thus calculated with the following simple equations:

(1) $$C_{L,eff} = C_L + C_{F,L}$$
(2) $$C_{F,ex} = C_{F,inf} - C_D$$

The main advantage of the ACL-boosted method is that it skips the initial temporal development of the (steady-state) slipstream via an initial simulation with the ACD model. In order to verify extent of this advantage, the initial slipstream development process was analysed. The development of the effective lift coefficient $C_{L,eff}$ is plotted in Figure 11.
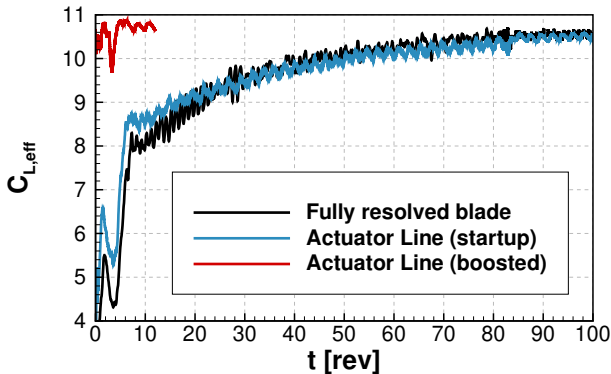
FIG 11. Comparison of slipstream development process for different unsteady propeller methods: development of lift coefficient over time

For the two simulations that capture the temporal development of the slipstream, a time step of $4°$ was selected in order to accelerate the simulation and to reduce the computation cost. In blocks of 20 revolutions, additional simulations are run with the fine time step of $0.5°$, using the respective solution of the $4°$ simulation as a starting point. For both the ACL case and the fully resolved case, a periodic state was reached in the "80-100 rev" block. In total, around 85-90 revolutions are required until a periodic state is reached when starting from a zero-thrust case, compared to the 8 revolutions seen for the ACL-boosted case.

In order to compare the steady-state performance predicted by each method, the integral performance parameters were averaged over the last 4 revolutions. The results are plotted in Table 5.

Method	$C_{L,eff}$	$C_{F,ex}$	C_P
Fully resolved blades	10.57	2.68	0.290
Actuator Line (startup)	10.52	2.52	0.245
Actuator Line (boosted)	10.74	2.62	0.244
Actuator Disk (unsteady)	10.68	2.72	0.245

TAB 5. 4-revolution average of integral performance coefficients for different propeller methods

For additional comparison, a simulation analogous to the ACL-boosted case was run with the ACD model. The same setup was used for this case, running 12 revolutions at the same time step of $0.5°$. As a result, the advantage of this simulation compared to the ACL-boosted simulation, e.g. in terms of computation cost, is small compared to the loss of unsteady effects. However, the goal of this simulation is to showcase that steady-state effects are dominant regarding the resulting integral performance parameters, as can be seen in Table 5, where the deviation between the ACL-boosted case and the ACD case are small.

9

The effective lift $C_{L,eff}$ results of the three unsteady methods results are within a span of $<2.5\%$, while the span of $C_{F,ex}$ is larger with $<6.5\%$. As a reminder, $C_{F,ex}$ represents a subtraction of two parameters (thrust and drag) and thus small individual errors can be magnified. The ACL-boosted case predicts more beneficial values of all parameters than the ACL-startup case. However, it is possible that the values would converge with more simulation run time. An unusually large deviation of up to $<19\%$ (usually $<5\%$) is found for the power coefficient C_P, where the fully resolved case predicts a significantly larger power requirement than the ACL cases. Two possible explanations for this are:

- At these large inflow angles the propeller polars used as input for the ACL are outside the optimal operation range and thus fail with regard to the local drag prediction and thus the power prediction.
- The additional unsteady effect (see section 3.3.1) has an upstream influence on the propeller, e.g. due to increased losses in the slipstream.
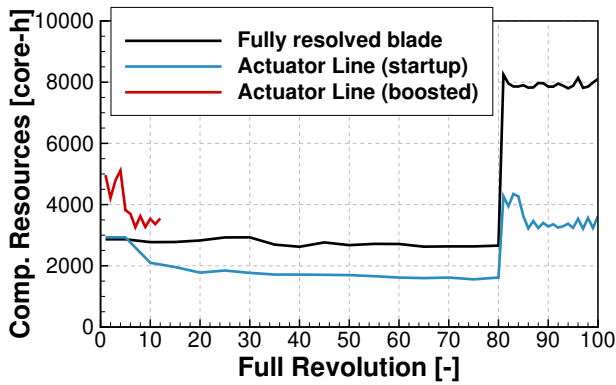
FIG 12. Comparison of computation cost for different unsteady propeller methods: development of core-h/rev over time

Next, the computational requirements of the three unsteady methods are compared. The development of the computation cost per propeller revolution is plotted in Figure 12. As was previously discussed, the simulations that examine the full slipstream development have a significantly longer run time, where the first part of the simulation is run at a time step of $4°$. Here, the simulation was run in groups of 5 revolutions, leading to the lower resolution of the curve. The jump in computation cost at 80 revolutions is then caused by the switch in time step to $0.5°$. Interestingly, the drop in computation cost after about 5 revolutions at the fine time step observed with both ACL simulations (see also Figure 7) is not present in the fully resolved simulation.

Propeller method	Iterations	Core-hours
Fully resolved blades	10,629,409	377,702
Actuator Line (startup)	5,755,365	214,508
Actuator Line (boosted)	1,264,948	47,190

TAB 6. Required computational resources by different unsteady propeller methods

The integral of the individual curves in Figure 12 represents the respective total computation cost. The specific values are also listed in Table 6. As expected, the fully resolved simulation presents the largest computation cost of the three methods. By switching to the ACL method, while still capturing the full slipstream development, the computation cost can be reduced by about 43%. A further large reduction of about 78% is possible by skipping the slipstream development process via an initial ACD simulation (ACL-boosted). Overall, the ACL-boosted method requires only about 12.5% of the computational resources of the most expensive fully resolved blade method, while predicting similar results (except for the power coefficient C_P, as discussed previously).

3.3.1. Additional effect with fully resolved blades

In the fully resolved blade simulation an additional unsteady effect is observed that is not present in the ACL simulations, see Figure 10, and that was therefore not discussed in section 3.2. The process behind this additional effect is illustrated in Figure 13, showcasing the development of the vortex in a representative Z=const cut at wing height (central section). The process can be described as follows:

- Starting condition (Figure 13a): Two vortices were merged into a single "double-vortex" (1+2). The following two vortex stencils (3 and 4) move in flow direction towards the wing.
- Translation/deformation step (Figure 13b): Vortex 3 is influenced by multiple factors, indicated by red arrows. Due to the proximity to the wing, a stagnation of the flow is observed, leading to a deceleration of the axial movement of vortex 3 as well as a momentum shift in spanwise direction ("outwards"). At the same time, the double vortex 1+2 and vortex 4 induce a deformation of vortex 3.
- Mixing step (Figure 13c): Due to the stagnation from the wing, the deformed vortex 3 is now in very close proximity to the following vortex 4, leading both vortices to mix and merge to a new double-vortex 3+4.
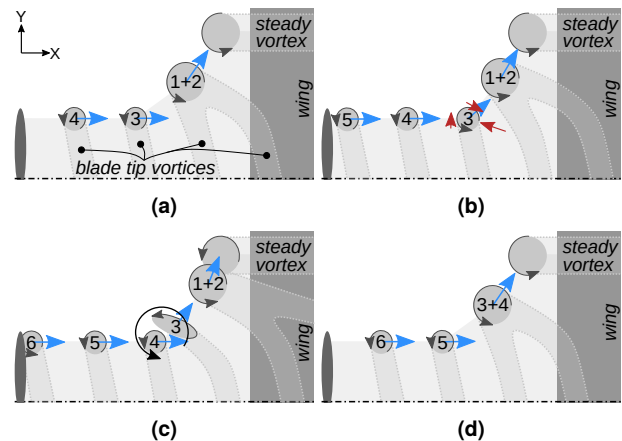- Loop ends, back to starting condition (Figure 13d).

FIG 13. Illustration of the additional effect in the central vortex section of the fully resolved simulation

The described process is physically plausible and is therefore discussed in the present paper. However, it is the authors' assessment that for the present case the more realistic vortex structure is the one predicted by the ACL simulations. The strength of the blade tip vortices in the fully resolved case and the ACL cases was compared: while previous investigations have shown that the ACL under-predicts the strength of blade tip vortices [3], in this case the ACL simulations actually showcase the stronger blade tip vortices. This can be explained by the fact that the ACL simulation has a clean, structured grid in the propeller wake, whereas in the fully resolved blade simulation the blade tip vortex needs to travel through two dissipative layers: 1) a layer of tetrahedral cells connecting the blade boundary layer to the CHIMERA overlap region and 2) the CHIMERA overlap region itself, where flow variables are interpolated, leading to additional dissipation. This highlights an additional advantage of the boundary condition based models such as the ACL: creating a good, low-dissipation mesh is significantly easier, since the complex geometry of the blade does not need to be accounted for in the mesh. Ultimately, the reduced vortex strength leads to reduced stability of the vortex and thus a higher susceptibility to vortex mixing, as observed in this secondary effect. It is therefore also possible that this effect is seen physically in a case with inherently lower vortex strength (i.e. with lower thrust settings).

4. SUMMARY

Unsteady propeller-wing interaction effects of a distributed propulsion system in a high-lift case were investigated via unsteady numerical simulations. The numerical setup was varied with two significant parameters: the turbulence model and the time step. Two different propeller representation methods were employed and compared: fully resolved blades and the boundary condition based Actuator Line model. The unsteady effects were isolated from the steady-state effects and detailed. The initial slipstream development process was examined. The investigation resulted in the following primary conclusions:

- Of the investigated one- and two-equation turbulence models, the Spalart–Allmaras turbulence model without rotation correction (SA-neg) offers the best mix of low numerical dissipation and computation cost.
- Decreasing the time step leads to convergence of the obtained results. Starting with a time step equivalent to $2°$ of blade rotation per step the changes become very small. The lowest investigated time step corresponds to $0.5°$ of blade rotation.
- A time step equivalent to $4°$ of blade rotation per step is required in order to capture continuous discrete blade tip vortices.
- Decreasing the time step by a factor of 8 effectively doubles the computation cost.
- The unsteady effects are dominated by the influence of the blade tip vortices and their behaviour.

- Blade tip vortex behaviour can be divided into two categories: the upper and lower vortex segments are characterized by straight forward propagation in flow direction. The central segment is characterized by strong interaction with the wing, "wrapping around" the wing and the merging of multiple stencils into a single, steady-state streamwise vortex.
- Local pressure fluctuations on the wing surface are caused by the blade tip vortices and the blade wake sheet. They are strongest on the descending blade side, behind the propeller tip.
- Steady-state effects are dominant for the integral performance of the propeller-wing system.
- The fully resolved blade simulation predicts an additional, physically plausible effect. However, this effect is likely caused by weakened blade tip vortices.
- In this high-lift case, around 85-90 propeller revolutions are required to obtain a developed slipstream.
- The Actuator Line method, when restarted from a steady-state Actuator Disk simulation and thus skipping the slipstream development process, requires only about 12.5% of the computational resources as the fully resolved blade method.

ACKNOWLEDGMENTS

Contact address:

mario.firnhaber-beckers@iag.uni-stuttgart.de

References

[1] Leo L. M. Veldhuis. *Propeller Wing Aerodynamic Interference*. PhD thesis, Delft University of Technology, 2005.

[2] Tomas Sinnige. *Aerodynamic and Aeroacoustic Interaction Effects for Tip-Mounted Propellers: An Experimental Study*. PhD thesis, Delft University of Technology, 2018. DOI: 10.4233/uuid:214e1e9a-c53e-47c7-a12c-b1eb3ec8293b.

[3] T.C.A. Stokkermans. *Aerodynamics of Propellers in Interaction Dominated Flowfields: An Application to Novel Aerospace Vehicles*. PhD thesis, Delft University of Technology, 2020. DOI: 10.4233/uuid:46178824-bb80-4247-83f1-dc8a9ca7d8e3.

[4] Mário Firnhaber Beckers, Michael Schollenberger, Thorsten Lutz, Dustin Bongen, Rolf Radespiel, Juan L. Florenciano, and David E. Funes-Sebastian. Numerical investigation of high-lift propeller positions for a distributed propulsion system. *Journal of Aircraft*, 60(4):995–1006, 2023. DOI: 10.2514/1.C037248.

[5] Mário Firnhaber Beckers, Maximilian Kern, Michael Schollenberger, and Thorsten Lutz. *CFD-based Studies of Propeller Sizing and Operation Settings for High-Lift Applications of Distributed Propulsion*, AIAA AVIATION 2023 Forum. 2023. DOI: 10.2514/6.2023-3396.

[6] Hyun D. Kim, Aaron T. Perry, and Phillip J. Ansell. *A Review of Distributed Electric Propulsion Concepts for Air Vehicle Technology*, *2018 AIAA/IEEE Electric Aircraft Technologies Symposium*. 2018. DOI: 10.2514/6.2018-4998.

[7] R.R. Duivenvoorden, Noah Suard, T. Sinnige, and L.L.M. Veldhuis. *Experimental Investigation of Aerodynamic Interactions of a Wing with Deployed Fowler Flap under Influence of a Propeller Slipstream*, AIAA AVIATION 2022 Forum. 2022. DOI: 10.2514/6.2022-3216.

[8] Andre Ribeiro, Ramon Duivenvoorden, and Diogo Martins. *High-Fidelity Simulations of Propeller-Wing Interactions in High-Lift Conditions*, *AIAA AVIATION 2023 Forum*. 2023. DOI: 10.2514/6.2023-3541.

[9] Robert Nederlof, Daniele Ragni, and Tomas Sinnige. *Experimental Investigation of the Aerodynamic Performance of a Propeller at Positive and Negative Thrust and Power*, AIAA AVIATION 2022 Forum. 2022. DOI: 10.2514/6.2022-3893.

[10] Jatinder Goyal, Tomas Sinnige, Francesco Avallone, and Carlos Ferreira. *Aerodynamic and Aeroacoustic Characteristics of an Isolated Propeller at Positive and Negative Thrust*, *AIAA AVIATION 2021 Forum*. DOI: 10.2514/6.2021-2187.

[11] Karen Deere, Sally Viken, Melissa Carter, Jeffrey Viken, Michael Wiese, and Norma Farr. Computational analysis of powered lift augmentation for the leaptech distributed electric propulsion wing. 06 2017. DOI: 10.2514/6.2017-3921.

[12] Michael D. Patterson. *Conceptual Design of High-Lift Propeller Systems for Small Electric Aircraft*. PhD thesis, Georgia Institute of Technology, 2016.

[13] Donato de Rosa, Elisa Morales Tirado, and Giuseppe Mingione. Parametric investigation of a distributed propulsion system on a regional aircraft. *Aerospace*, 9(4), 2022. ISSN: 2226-4310. DOI: 10.3390/aerospace9040176.

[14] Till K. Lindner, Jonas Oldeweme, Peter Scholz, and Jens Friedrichs. *Experimental Propeller Placement Analysis for a Distributed Propulsion Wing Section in High Lift Configuration*, *AIAA AVIATION 2023 Forum*. 2023. DOI: 10.2514/6.2023-3539.

[15] Alex Gothow, Julien Weiss, Andreas Bardenhagen, Dominique P. Bergmann, Jan Denzel, and Andreas Strohmayer. *Experimental Parameter Study of Distributed Electric Propulsion on a 2D Wing Model in High-Lift Configuration*, *AIAA AVIATION 2023 Forum*. 2023. DOI: 10.2514/6.2023-3540.

[16] Dustin Bongen, Mário Firnhaber Beckers, Michael Schollenberger, Dominique P. Bergmann, Thorsten Lutz, Alex Gothow, Mahmod Saeed, Julien Weiss, Andreas Bardenhagen, and Rolf Radespiel. *Simulation of a Distributed Propulsion System in a Wind Tunnel*, *AIAA AVIATION 2022 Forum*. 2021. DOI: 10.2514/6.2022-3818.

[17] Robin Wickersheim, Manuel Keßler, and Ewald Krämer. *Assessment of the Actuator Line Method for the Aeroacoustic Simulation of Distributed Electric Propulsion*, *AIAA AVIATION 2023 Forum*. 2023. DOI: 10.2514/6.2023-4181.

[18] Michael Schollenberger, Mário Firnhaber Beckers, and Thorsten Lutz. *Validation of ACD and ACL propeller simulation using blade element method based on airfoil characteristics*, Wolfgang E. Nagel, Dietmar H. Kröner, and Michael M. Resch, editors, *High Performance Computing in Science and Engineering '21*, pages 367–380. Springer International Publishing, Cham, 2023. ISBN: 978-3-031-17937-2. DOI: 10.1007/978-3-031-17937-2$_2$2.

[19] Michael Schollenberger, Thorsten Lutz, and Ewald Krämer. *Boundary Condition Based Actuator Line Model to Simulate the Aerodynamic Interactions at Wingtip Mounted Propellers*, pages 608–618. 01 2020. ISBN: 978-3-030-25252-6. DOI: 10.1007/978-3-030-25253-3$_5$8.

[20] Dieter Schwamborn, Thomas Gerhold, and Ralf Heinrich. *THE DLR TAU-CODE: RECENT APPLICATIONS IN RESEARCH AND INDUSTRY*, *ECCOMAS CFD 2006 CONFERENCE*. 2006.

[21] Ben Thornber, A. Mosedale, Dimitris Drikakis, David Youngs, and R.J.R. Williams. An improved reconstruction method for compressible flows with low mach number features. *Journal*

of Computational Physics, 227:4873–4894, 05 2008. DOI: 10.1016/j.jcp.2008.01.036.

[22] Marco Burnazzi and Rolf Radespiel. Design and analysis of a droop nose for coanda flap applications. *Journal of Aircraft*, 51(5):1567–1579, 2014. DOI: 10.2514/1.C032434.

[23] Axel Raichle, Stefan Melber-Wilkending, and Jan Himisch. A new actuator disk model for the tau code and application to a sailplaine with a folding engine. volume 96, 10 2007. ISBN: 978-3-540-74458-0. DOI: 10.1007/978-3-540-74460-3$_7$.

[24] U. Burggraf, M. Kuntz, and B. Schöning. *Implementation of the Chimera Method in the Unstructured DLR Finite Volume Code Tau*, Wolfgang Nitsche, Hans-Joachim Heinemann, and Reinhard Hilbig, editors, *New Results in Numerical and Experimental Fluid Mechanics II: Contributions to the 11th AG STAB/DGLR Symposium Berlin, Germany 1998*, pages 93–100. Vieweg+Teubner Verlag, Wiesbaden, 1999. ISBN: 978-3-663-10901-3. DOI: 10.1007/978-3-663-10901-3$_1$3.

[25] Cadence. Pointwise homepage. version in this paper: V18.4 r2. https://www.pointwise.com/, 2023.

[26] Steven Allmaras, Forrester Johnson, and Philippe Spalart. Modifications and clarifications for the implementation of the spalart-allmaras turbulence model. *Seventh International Conference on Computational Fluid Dynamics (ICCFD7)*, pages 1–11, 01 2012.

[27] Michael L. Shur, Michael K. Strelets, Andrey K. Travin, and Philippe R. Spalart. Turbulence modeling in rotating and curved channels: Assessing the spalart-shur correction. *AIAA Journal*, 38(5):784–792, 2000. DOI: 10.2514/2.1058.

[28] F. R. Menter. Two-equation eddy-viscosity turbulence models for engineering applications. *AIAA Journal*, 32(8):1598–1605, 1994. DOI: 10.2514/3.12149.

[29] David C. Wilcox. Reassessment of the scale-determining equation for advanced turbulence models. *AIAA Journal*, 26(11):1299–1310, 1988. DOI: 10.2514/3.10041.